JOURNAL OF AIRCRAFT
Vol. 44, No. 1, January–February 2007

Reynolds Number Effects on Off-Design Stability and Control Characteristics of Supersonic Transports

Lewis R. Owens* and Richard A. Wahls†
NASA Langley Research Center, Hampton, Virginia 23681
Michael B. Elzey‡
Boeing Commercial Airplane Group, Seattle, Washington 98124
and
Marvine P. Hamner§
LeaTech, LLC, Frederick, Maryland 21703

DOI: 10.2514/1.22519

A high Reynolds number wind-tunnel test was conducted to assess Reynolds number effects on the stability and control characteristics of a realistic, second-generation supersonic transport concept. The testing included longitudinal and lateral/directional studies at transonic and low-speed, high-lift landing conditions across a range of Reynolds numbers from that available in conventional wind tunnels to near-flight conditions. Results presented focus on Reynolds number sensitivities of the stability and control characteristics at Mach 0.30 and 0.95 for a configuration including empennage. The angle of attack where the pitching-moment departure occurred increased with higher Reynolds numbers for both the landing and transonic configurations. Stabilizer effectiveness and directional stability increased with the Reynolds number for both configurations. The landing configuration without forebody chines exhibited a large yawing-moment departure at high angles of attack and zero sideslip that varied with increasing Reynolds numbers. This departure characteristic nearly disappeared when forebody chines were added. The landing configuration's rudder effectiveness also exhibited sensitivities to changes in Reynolds number. This study extends the existing Reynolds number database for supersonic transports operating at subsonic conditions.

Nomenclature

C_D	=	drag coefficient
CI_{95}	=	95% confidence interval
C_L	=	lift coefficient
C_l	=	rolling-moment coefficient referenced to 0.50 mean aerodynamic chord
C_M	=	pitching-moment coefficient referenced to 0.50 mean aerodynamic chord
$C_{M_{C_L}}$	=	longitudinal stability derivative
$C_{M_\delta,\text{stab}}$	=	stabilizer effectiveness, per degree
C_{M_0}	=	pitching-moment coefficient at $C_L = 0$
C_n	=	yawing-moment coefficient referenced to 0.50 mean aerodynamic chord
C_{n_β}	=	directional stability derivative, per degree
$C_{n_\delta,\text{rud}}$	=	rudder effectiveness, per degree
C_Y	=	side-force coefficient
c	=	local chord length, in.
h_{np}	=	neutral point, fraction of mean aerodynamic chord
L/D	=	lift-to-drag ratio
M	=	Mach number
P_T	=	total pressure, psia
q	=	dynamic pressure, psf
Rn	=	Reynolds number based on mean aerodynamic chord
r	=	local leading-edge radius, in.
T_T	=	total temperature, °F
$t_{\max}$	=	local maximum airfoil thickness, in.
α	=	angle of attack, deg
β	=	angle of sideslip, deg
ε	=	downwash angle, deg
η	=	nondimensional semispan station

Presented as Paper 0417 at the 40th AIAA Aerospace Sciences Meeting & Exhibit, Reno, NV, 14–17 January 2002; received 17 January 2006; revision received 18 July 2006; accepted for publication 26 July 2006.

*Aerospace Engineer, Flow Physics and Control Branch. Senior Member AIAA.
†Assistant Head, Configuration Aerodynamics Branch. Associate Fellow AIAA.
‡Senior Principal Engineer (Retired).
§Principal. Senior Member AIAA

Introduction

GROUND-TO-FLIGHT scaling remains one of many challenges facing today's designers of aerospace vehicles. The goal of ground-to-flight scaling is the preflight prediction of multiple key aerodynamic characteristics with sufficient accuracy to meet both performance guarantees and certification requirements. The designer must strive to know the performance of a vehicle with high confidence before flight, thus enabling optimal design trades to eliminate costly fixes to the aircraft after initial flight tests.

Specific challenges, experiences, and suggested approaches to ground-to-flight scaling have been documented extensively over the years for a variety of vehicle classes [1,2]. Reynolds number effects are among many of the factors affecting successful ground-to-flight scaling [3–5]. The Reynolds number is the ratio of inertial to viscous forces, and is a primary aerodynamic scaling parameter used to relate subscale wind-tunnel models to full-scale aircraft in flight. The challenge of Reynolds number scaling increases with the size of a full-scale aircraft as the Reynolds number increment between that obtainable in conventional wind tunnels and at flight conditions expands. Additionally, the challenge for both wind tunnel and computational approaches increases as flow features become dominated by viscous-sensitive phenomena such as boundary-layer transition, shock/boundary-layer interaction, and separation onset and progression.

The present investigation was conducted in support of NASA's High Speed Research (HSR) Program conducted from 1993–1999 [6]. The objective of this program was to develop critical high-risk airframe and propulsion technologies to enable industry development of an economically viable and environmentally acceptable second-generation, high-speed civil transport (HSCT). The

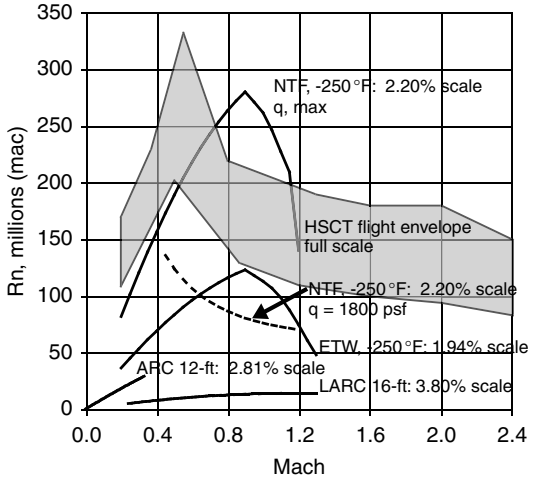

Fig. 1 Nominal HSCT mission profile and wind-tunnel capabilities (model scale adjusted to test section size, 2.2% scale in the NTF is the baseline size). ARC

aerodynamic performance elements of this program included tasks encompassing not only the challenge of efficient supersonic cruise flight, but also off-design challenges of efficient transonic cruise and acceleration and quiet high-performance takeoff and landing [7]. The objective was the development of practical concepts and design and analysis methods to allow the HSCT to operate safely and efficiently. To reduce risk in the vehicle design process, a study was developed to identify and test vehicle components that would contribute to stability and control differences between the full-scale vehicle and small-scale wind-tunnel models. Figure 1 shows the nominal flight envelope for the baseline reference configuration used in the HSR program and a comparison to the capability of several wind tunnels [Ames Research Center (ARC) 12-ft tunnel, European Transonic Wind Tunnel (ETW), and Langley Research Center's (LARC's) National Transonic Facility (NTF) 16-ft tunnel]. The baseline reference configuration, known as reference H, was provided by Boeing and represented a Mach 2.4, 300-passenger aircraft with a 5000 n mile range. This configuration provided a representative model for this class of vehicle on which to study the Reynolds number effects affecting the stability and control characteristics.

A series of wind-tunnel tests was conducted in the NTF [8–11] at the LARC across a wide range of Reynolds numbers. The Reynolds numbers ranged from that available in conventional wind tunnels to near-flight condition at subsonic and transonic Mach numbers. The tests included longitudinal and lateral/directional studies with and without an empennage at transonic and low-speed, high-lift landing conditions. This paper presents results focused on the Reynolds number sensitivities of the stability and control characteristics at Mach numbers of 0.30 and 0.95 for a complete HSCT aircraft configuration including empennage.

Experimental Approach

Model Description

The wind-tunnel model is a 2.2% scale representation of the HSR baseline configuration known as reference H. Although the model without the empennage was previously tested in the NTF during the HSR program [12–14], the present paper focuses on results obtained for the full configuration with empennage. Figure 2 shows a planform and side view sketch of the model with several reference locations noted.

The model has a cranked-delta wing planform with an aspect ratio of 2.367, a span of 34.22 in., and a mean aerodynamic chord (MAC) of 22.71 in. The inboard wing ($\eta \leq 0.522$) has a blunt ($r/c \sim 0.0025$ to 0.0030), subsonic leading edge (LE) with a sweep change from 76 to 68.5 deg at $\eta = 0.226$, a twist varying from approximately 1 deg near $\eta = 0.10$ deg to -2 deg near $\eta = 0.50$, and variable thickness ratio ($t_{\max}/c$) from 0.043 to 0.024. The outboard supersonic LE is sharp, swept 48 deg, has a constant twist of -1.6 deg for $\eta \geq 0.65$,

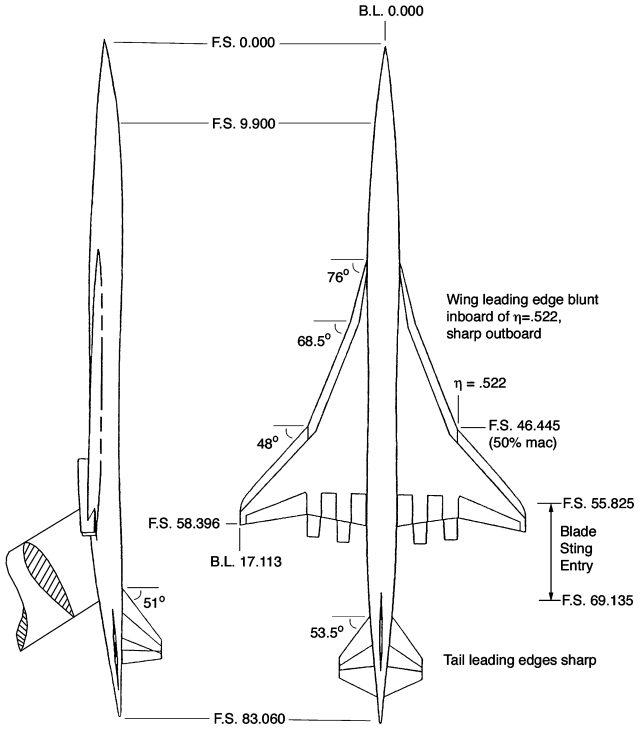

Fig. 2 Model sketch with reference locations (linear dimensions in inches).

and a constant thickness ratio of 0.024. The reference area for the model is 494.78 in.^{2}. The model fuselage tapered in the rear such that the upper surface was straight, whereas the lower surface sloped upward to close the fuselage in the side view (see Fig. 2). The overall body length was 83.060 in. Table 1 provides several important ratios relating the model size to the NTF test section.

The model has multiple inboard LE and trailing edge (TE) parts and multiple outboard wing panels, each with different LE and TE deflections. It also included four detachable, 8.43-in.-long, constant internal diameter (1.236 in.), circular flow-through nacelles with boundary-layer diverters located between the wing and nacelle. The inboard nacelles are rigged with toe-in and pitch (nose down) angles of 1 and 4.17 deg, respectively; the outboard nacelles are rigged with toe-in and pitch angles of 2.4 and 2.84 deg, respectively. The rigging of the engine nacelles resulted from the aerodynamic optimization process used in the design of this configuration. The multiple LE and TE parts in combination with the multiple outboard panels enabled testing of a variety of configurations including the supersonic cruise, takeoff, landing, stall recovery, and transonic cruise configurations. All results presented are for the transonic cruise and landing wing configurations with the nacelle/diverters installed. Table 2 includes wing flap deflections for these two configurations.

A forebody chine for the reference H geometry was tested with the high-lift landing configuration only. The chine LE (swept 60 deg) was located at fuselage station (FS) 9.900, and the chine semispan was 0.265 in. from the side of the body. The chine root chord was 1.98 in. and it had a tip chord of 1.367 in.

The model's horizontal tails (left and right) had an exposed area of 48.672 in.^{2} and an aspect ratio of 1.845 (based on exposed area and span). The horizontal tail span was 9.476 in. The LE sweep was 53.5 deg and the TE sweep was -27.4 deg. The airfoil section was a wedge-slab-wedge type.

Table 1 Model size relative to the NTF test section

Ratios	Values
Model wing reference area to NTF cross-sectional area	0.0515
Model span to NTF test section width	0.3478
Model frontal area to NTF cross-sectional area ($\alpha = 0$ deg)	0.0022

Table 2 Wing flap configurations presented

Designation	LE deflection, inboard/outboard	TE deflection, inboard/outboard
Landing	30/30 deg	20/20 deg
Transonic cruise	0/10 deg	0/3 deg

The model's vertical tail had an exposed area of 28.656 in.^{2} and an aspect ratio of 0.869 (based on exposed area and span). The vertical tail span was 4.990 in. The LE sweep was 51 deg and the TE sweep was −11.5 deg. The airfoil section was also a wedge-slab-wedge type. Two vertical tails were built, one with a nondeflected rudder and the other with a +30- deg rudder deflection (TE toward the left wing). The rudder had an exposed area of 7.776 in.^{2}, which is included in the vertical tail exposed area previously described. The rudder hinge line was a vertical line located at FS 73.618. The tip chord of the rudder is 47.5% of the vertical tail tip chord, and the rudder root chord is 22.08% of the vertical tail root chord. The rudder deflection was only tested at the low-speed conditions.

The model was designed and constructed specifically for testing in the cryogenic, pressurized conditions of the NTF. The nondeformed model shape was that of the Mach 2.4 cruise design point. This shape was designed using aerodynamics and structures theory, but did not account for any potential 1-g flight deformations. The model was built of maraging steel with a surface finish of 8–16 μin. (root mean square) and a contour tolerance of ±0.005 in. The model is shown in Fig. 3 mounted in the NTF test section on a lower-swept blade sting, which has a NACA 0012 airfoil section normal to the blade sting's swept LE. The sting mounts to a 6-deg offset stub sting, which in turn mounts to the facility arc sector resulting in a model α range from −4 to 24 deg. The β range varied depending on the angle-of-attack setting. At lower α, β varied between −12 and 12 deg. At higher α, β was limited to a range of −8 to 8 deg.

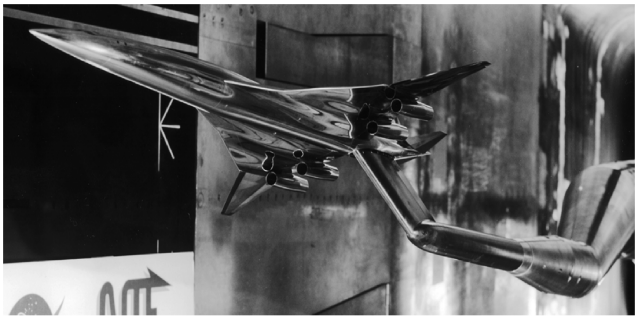

a) Front 3/4 view

b) Side view

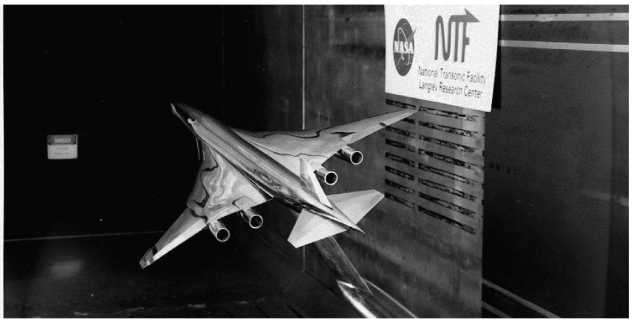

c) Rear 3/4 view

Fig. 3 HSR reference H model in the NTF (2.2% model scale).

Model Support System

Testing on a blade-sting support in sideslip is not an ideal way to obtain lateral/directional data, especially if the blade is not aligned with the freestream flow. However, the research goal of trying to model the aftbody closure with minimal geometry modification for accommodating the support sting led to the use of a blade-sting support. The blade portion of this sting in sideslip produced a pressure field on the aftbody and vertical tail, which introduced a bias from a free air configuration. A comparison of the directional stability was made at low Reynolds number for a similar configuration with a single post mounting system tested in NASA LARC's 14 by 22 ft subsonic tunnel. This comparison showed that the NTF measured directional stability was somewhat higher, but it is also recognized that the post mount also caused some interference. From this comparison, the NTF data were assumed to have some unknown level of bias in the absolute data levels that are consistent with standard sideslip testing techniques. However, steps were taken to make the observed Reynolds number effects be primarily indicative of changes in the model flowfield only. Boundary-layer transition trip strips were placed near the leading edge of the blade sting to try and minimize the change in this interference effect with the Reynolds number. In addition, directional derivatives were calculated over a limited β range ($-4 \text{ deg} < \beta < 4 \text{ deg}$) in an attempt to minimize the blade-sting interference effect.

The entry point of the blade sting into the fuselage is shown generally in Fig. 2. The nonmetric blade sting needed a clearance gap to prevent fouling as the model/balance deflected under load. An unsealed gap would have allowed flow to enter the fuselage cavity and thus would have affected the measured forces and moments. Sealing this gap without affecting the forces/moments was a challenging process that required some development work at the beginning of the test. More discussion about the seal development process is included in [15]. In the end, after much effort, data were obtained free of any significant seal interference effects.

Instrumentation

Aerodynamic force and moment data were obtained with an internal, unheated, six-component, strain gauge balance. The balance used was one of the NTF-113 class balances having the load capacity and accuracy shown in Table 3. An internal, heated accelerometer package was used to measure the onboard angle of attack for $\beta = 0$ deg α sweeps; quoted accuracy of the package under smooth operating wind-tunnel conditions is ±0.01 deg [16]. For sideslip conditions, arc sector measured pitch and roll angles plus calibrated sting bending (including nonmetric bending from blade loading) were used to determine α and β. The onboard accelerometer used could not measure angles out of the tunnel vertical plane of symmetry. Angles measured using the arc sector angles plus sting-bending technique are not as accurate as those measured directly by an onboard accelerometer, but are generally considered of the same order of accuracy (α and β uncertainty less than ±0.1 deg).

The model was instrumented with 17 aftbody pressures distributed circumferentially at FS 65.306 and 6 pressures distributed in a row on the port side (45 deg up from bottom dead center) just below the horizontal tail location. These pressures were used for a limited computational study [17] (Euler calculations) that investigated the blade-sting interference effects for symmetric flow conditions only (no sideslip). This computational study showed a small lower-surface compression increase in the wing TE region near the blade-

Table 3 Quoted NTF-113 balance capacity and accuracy values

Component	Full-scale load	Nominal accuracy 95% confidence
Normal, lb	±6500	±0.09% full scale
Axial, lb	±400	±0.33% full scale
Side, lb	±4000	±0.19% full scale
Pitch, in. · lb	±13, 000	±0.11% full scale
Yaw, in. · lb	±6500	±0.23% full scale
Roll, in. · lb	±9000	±0.35% full scale

sting entry, which provided a small interference effect at transonic conditions. Cavity pressures were also measured just inside the model near the blade-sting seal. These pressures were used to monitor the integrity of the seal during testing. None of the pressure data obtained during these tests will be presented.

The primary measured flow variables include both the total and static pressures and the total temperature. Mach number, Reynolds number, and q are calculated from these measured parameters. The tunnel Mach number, Reynolds number, and q have uncertainty levels of approximately ± 0.002, $\pm 0.5 \times 10^6$, and $\pm 1.5\%$ of reading, respectively. A complete description of these measurements and subsequent calculations is given in [18].

Data Reduction and Corrections

Information on the various instrumentation devices, the data acquisition and control computers, and the data reduction algorithms for the different measurement systems is provided in [18]. Standard balance, α, and tunnel parameter corrections have been applied. Note that the use of unheated balances in the cryogenic environment requires additional attention towards temperature compensation. The temperature compensation methods are designed to correct balance output due to thermal loads [18,19]. Body cavity pressures were used to calculate corrections to normal and axial forces and pitching moment to adjust the internal cavity pressure condition to freestream static. Nacelle internal drag and base pressure corrections were only applied to the $\beta = 0$ deg, α sweep data based on the measurements described previously in the wing/body testing [12–14]. The angle of attack was corrected for flow angularity (upflow only) by measurement of both upright and inverted model normal force data for a given configuration and flow condition. No consistent technique or data were available to characterize the tunnel side flow and no attempt was made to correct the flow angularity for this component. Wall and model support interference effects have not been accounted for in the data. The wall effects were minimized through model sizing (Table 1).

Test Conditions

The NTF allows testing across a wide range of Reynolds number from that available in conventional wind tunnels to near-flight conditions at subsonic and transonic Mach numbers. Tests of the 2.2% reference H model spanned M from 0.30 to 1.10, and Rn from 4.5 to 120×10^6 based on the MAC. The present paper focuses on both the low-speed and transonic regimes representative of landing and transonic cruise.

The landing configuration data were obtained at $M = 0.30$ for a Rn range from 4.5 to 90×10^6. The transonic cruise configuration data were obtained at $M = 0.95$ for a Rn range from 10.2 to 80×10^6. Figure 1 indicates the relationship of the NTF test conditions to flight, and Fig. 4 provides the NTF operational envelopes for $M = 0.30$ and $M = 0.95$ with specific test points identified. Full-scale flight Reynolds numbers are not obtained due to the large size of the full-scale aircraft, model size, and other limitations. For the $M = 0.30$ test condition, the Reynolds number was limited by the maximum P_T for reliable, sustainable cryogenic operations (i.e., 100 psia). The other limit was in part driven by the requirement of testing the same model at transonic conditions. Testing of the full configuration on a blade support sting imposed additional load limits at $M = 0.95$ ($q = 1800$ psf boundary in Fig. 1).

The goals of assessing Reynolds number scale effects and extrapolation to flight conditions required a series of intermediate

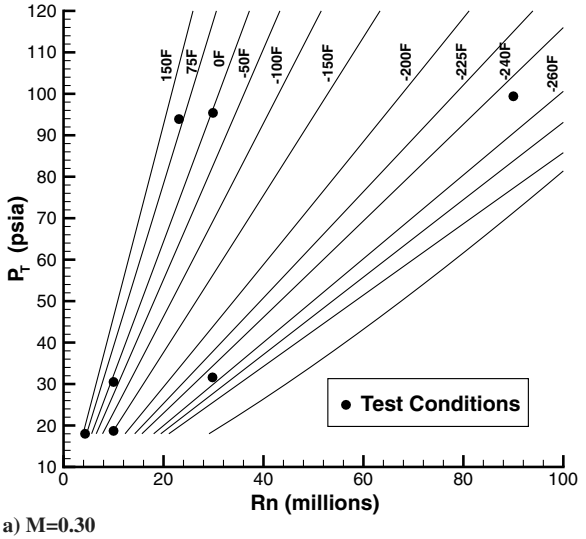

a) M=0.30

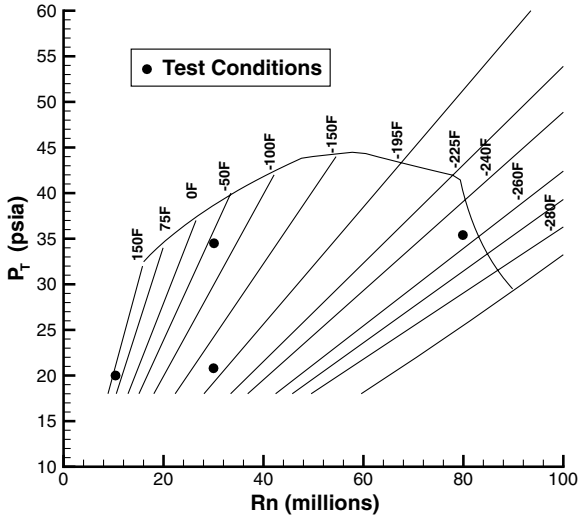

b) M=0.95

Fig. 4 NTF operational envelopes with T_T lines and test conditions.

conditions to better identify trends. As seen in Fig. 4, the desired Reynolds number range could not be covered at a constant P_T level (q level). However, the independent control of P_T, T_T, and fan speed in the NTF allow the isolation of pure viscous (Reynolds number) effects, pure static aeroelastic (q) effects, and pure compressibility (M) effects. Several conditions at each Mach number are used to isolate static aeroelastic effects from the Reynolds number effects, as shown in Fig. 4. During Reynolds number sweeps, the ratio of q to the model material modulus of elasticity E is held constant. This is done to maintain a constant, static aeroelastic state (q/E) due to the variability of the modulus of elasticity over the temperature range of the NTF.

Boundary-Layer Transition

No test data were obtained for any of these configurations with fixed transition on either the wing or tail surfaces. However, transition was consistently fixed on the forebody with a ring of carborundum grit located 1.5 in. from the nose and on the nacelle internal surface to facilitate the internal nacelle drag correction for the $\beta = 0$ deg α sweeps. The forebody grit ring was added early in the NTF HSR test program because of concerns that unsteady forebody aerodynamics caused by laminar boundary layers was responsible for model yaw dynamics at low angles of attack. After several tests, a structural dynamics study determined that unexpected tuning of frequency modes between the model and the tunnel support system

amplified the model yaw dynamics [20]. The HSR research team decided to continue using the forebody grit ring to be consistent with the earlier NTF HSR testing strategy. This forebody grit ring masked some of the Reynolds number effects at the lower α, but was assumed to have little effect at higher α. The nacelle internal surface boundary layers were also tripped to be consistent with previous HSR drag performance testing [14]. These internal nacelle trips may mask some of the Reynolds number effects and the impact on the stability and control characteristics is unknown. For this study, these effects were assumed minimal. As previously discussed, transition was also fixed on the blade sting to minimize the dependence of the blade-sting interference effect on Reynolds number variation. All trips were sized and located based on traditional criteria [21]. These boundary-layer trips were used for all experimental results presented in this paper.

Results and Discussion

The purpose of this paper is to document the Reynolds number sensitivities of stability and control characteristics for a relevant, supersonic transport configuration at conditions representative of landing and transonic cruise, $M = 0.30$ and 0.95, respectively. Note that in the discussion of these data, the baseline landing configuration has wing landing flap deflections (see Table 2), forebody chines, a vertical tail, and a horizontal stabilizer (stab) setting of 0 deg. The baseline transonic cruise configuration has wing transonic cruise flap deflections (see Table 2), a vertical tail, and a horizontal stab setting of 0 deg. Note that the transonic configurations were always tested without forebody chines during this investigation. The landing configuration was also tested with a vertical tail that included a rudder deflection.

Figure 5a presents representative longitudinal data for the landing configurations at a Rn of 90×10^6. The figure illustrates the basic longitudinal aerodynamic characteristics with different horizontal stabilizer configurations. Figure 5b presents similar data for the transonic cruise configurations at a Rn of 80×10^6. These data are shown to give the reader a general idea of the overall character of the forces and moments from which the longitudinal stability and control parameters were calculated. Note that the effects of adding and deflecting the stab are clearly seen in the pitching moment and L/D plots.

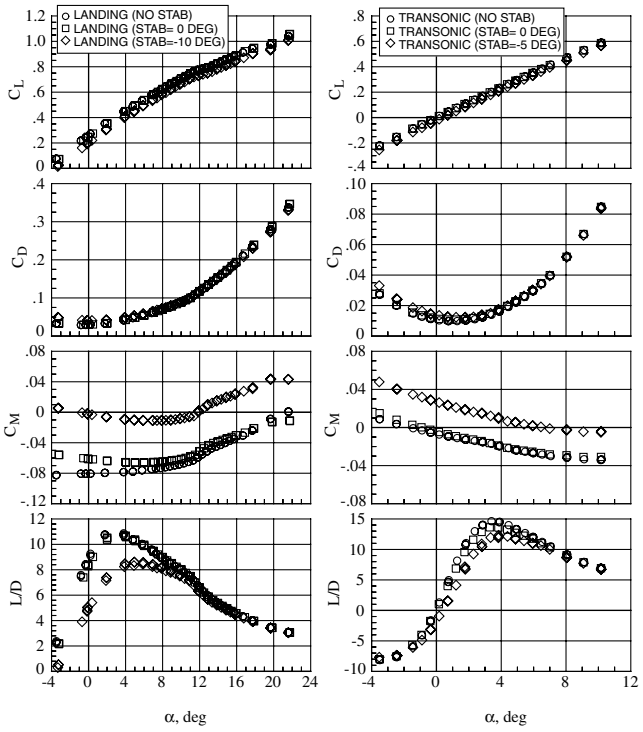

a) M=0.30, Rn=90 x 10^6 **b) M=0.95, Rn=80 x 10^6**

Fig. 5 Basic longitudinal force and moment data (no static aeroelastic correction).

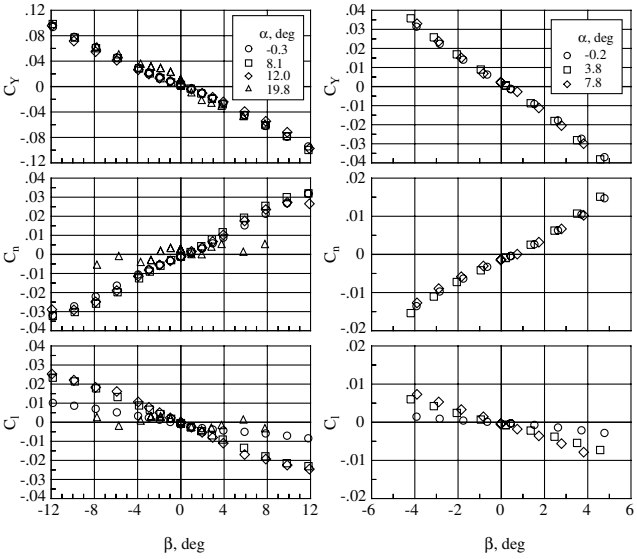

a) Landing (Vert on, Chine on), M=0.30, Rn=90 x 10^6 **b) Transonic (Vert on), M=0.95, Rn=80 x 10^6**

Fig. 6 Basic lateral/directional force and moment data (no static aeroelastic correction).

Figure 6a presents representative lateral/directional data for the landing configuration at various α and a Rn of 90×10^6. Figure 6b presents similar data for the transonic configuration at a Rn of 80×10^6. These data are shown to give the reader a general idea of the overall character of the forces and moments from which the directional stability and control parameters were calculated.

The acquired data include the combined effects of static aeroelastic deformation and Reynolds number effects. In general, addressing static aeroelastic effects is necessary as a means to isolate and more properly address pure Reynolds number effects [12–14]. However, the static aeroelastic corrections are not included for the data with β because only a very limited set of static aeroelastic data were acquired for these runs. If aeroelastic corrections were available, then corrections to that data were made whenever possible and the fact that aeroelastic corrections were made are noted in the appropriate figure captions.

Repeatability

Data presented herein were acquired across two wind-tunnel tests of the model within several months of each other. This section provides a list of short-term repeatability estimates (within test/Mach series) that are quantified in terms of a 95% confidence interval for each configuration as described in [22]. The 95% confidence interval is interpreted as the bounds about an estimated mean (average of multiple, repeat polars) that encompasses the true mean value with a chance of 95%. A number of repeat runs were obtained for longitudinal runs with $\beta = 0$ deg to provide the average values of the 95% confidence interval for each force and moment coefficient. Because only a few repeat runs were made for the lateral/directional data runs, the averages listed do not include any of these data. Table 4 lists these estimates of uncertainty for the longitudinal repeat runs.

Static Aeroelastic Effects

Achieving high Reynolds numbers approaching that characteristic of flight requires the manipulation of both the T_T and P_T, as seen in Fig. 4. As a result, the static aeroelastic deformation of the model (in particular, the wing) under load must be considered when attempting to isolate Reynolds number effects. Previous reports for high aspect ratio subsonic transport configurations have shown the static aeroelastic effects to be on the order of Reynolds number effects. Often these aeroelastic effects are opposite in sense to that of Reynolds number trends, thus masking the Reynolds number effects

Table 4 Average CI_{95} for each configuration for longitudinal repeat runs

	Landing	Transonic Cruise
C_L	±0.0014	±0.0020
C_D	±0.0003	±0.0004
C_M	±0.0003	±0.0007
C_Y	±0.0005	±0.0006
C_n	±0.0002	±0.0003
C_l	±0.0002	±0.0001

[23,24]. Like the subsonic transport configurations, the current low aspect ratio HSCT model is flexible under load, most notably on the thin outboard wing panel and empennage [12–14].

The effects of static aeroelastic wing and empennage bending were obtained with constant Reynolds number at high and low q test conditions, as shown in Fig. 4. Adjustments to remove the aeroelastic effects were made to the α sweep ($\beta = 0$ deg) data only because limited resources did not permit the acquisition of aeroelastic effects for β sweep runs. For the longitudinal data presented, the lift and pitching-moment coefficients were corrected to values that correspond to the rigid, nondeformed model shape. This correction was applied to these longitudinal data because the rigid, nondeformed model shape is frequently used in computational studies. The correction procedure is similar to that discussed in [12–14]. However, the correction procedure used in the current paper adjusted the coefficient data to the rigid model shape instead of the lowest dynamic pressure level as described in these references.

Reynolds Number Effects

The following discussion will examine the Reynolds number trends for pertinent longitudinal stability and control characteristics (with static aeroelastic corrections) and directional stability and control characteristics (without static aeroelastic corrections).

Longitudinal Characteristics

Figure 7 presents the Reynolds number effects on pitching-moment characteristics for both the landing and the transonic configurations. These data include corrections for static aeroelastic effects, thus providing better isolation of Reynolds number effects. In Fig. 7a, the landing configuration has the expected more negative C_{M_0} produced by the increased wing camber from the inboard/outboard wing flap deflections relative to the transonic configuration. The C_{M_0} is essentially constant as the Reynolds number increases. The landing configuration exhibits pitch stability up to a C_L of about 0.45. Above this C_L level, the stability degrades as the configuration experiences the typical high-attitude phenomenon associated with increasing outboard wing panel separations. The increase in Reynolds number delays the onset of the pitching-moment departure, but also causes that departure to progress more rapidly at even higher C_L values. Overall, the pitch stability appears to improve with increasing Reynolds number. Later, the discussion will look at the longitudinal stability as a function of the Reynolds number in greater detail.

The transonic configuration demonstrated a more positive C_{M_0} as compared with the landing configuration, which is produced by the smaller amount of wing camber associated with the outboard wing flap deflections. This C_{M_0} is also essentially insensitive to any variation in Reynolds number, as shown in Fig. 7b. The transonic configuration exhibits pitch stability up to a C_L of about 0.5, above which the nonlinear progression begins due to the same factors discussed previously for the landing configuration. At lower C_L values, the longitudinal stability is less sensitive to Reynolds number change for transonic conditions. As observed for the landing configuration, the model nose-up onset with C_L is delayed as the Reynolds number increases.

Some of the basic longitudinal stability and control parameters calculated from data (with static aeroelastic corrections) for the landing configurations are shown in Fig. 8. In the upper left portion of this figure, the wing induced downwash angle affecting the horizontal stabilizer's performance is shown as a function of the Reynolds number for specific α. As α increases, the downwash angle increases, because the inboard wing generates more lift, which results in a larger turning angle in the oncoming flow. The downwash angle increases slightly as the Reynolds number increases, which, presumably, is the result of more efficient turning of the flow by the wing and TE flaps. This efficiency increase is probably due to a combination of decreases in the wing boundary-layer thickness (local camber increase and healthier boundary-layer approaching flap) as well as improvements in the TE flap performance caused by local separation delays.

In the lower left plot of Fig. 8, the stabilizer effectiveness for the landing configuration is shown as a function of the Reynolds number. At each Reynolds number, the stabilizer effectiveness decreases as α increases, as expected. The data at $\alpha = 20$ deg are an exception to this trend, which is believed to be caused by the highly separated flowfield. A consistent pattern of stabilizer effectiveness emerges with the Reynolds number, if the $\alpha = 20$ deg data are ignored. At α of 8 and 12 deg, the stabilizer effectiveness increases on the order of 5% as the Reynolds numbers increase toward that of flight. These α are typical for the landing configuration. These results are consistent with the stabilizer effectiveness results for subsonic transports [25]. The results in [25] compare the stabilizer effectiveness calculated from wind-tunnel data (low Reynolds number), flight data (high Reynolds number) and inviscid analyses (infinite Reynolds number). This comparison shows an increase in stab effectiveness with increasing Reynolds number similar to that seen in the Fig. 8 data discussed previously. In [25], viscous effects

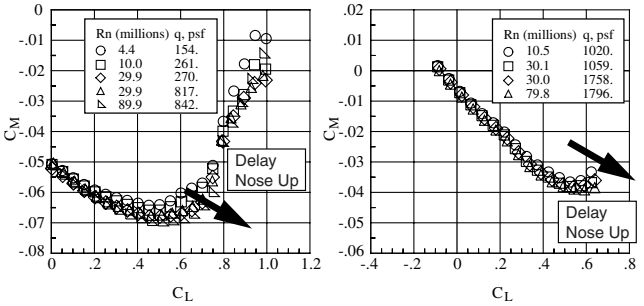

a) M=0.30, Landing (Stab=0°) **b) M=0.95, Transonic (Stab=0°)**

Fig. 7 Reynolds number effect on pitching moment (corrected for static aeroelastics).

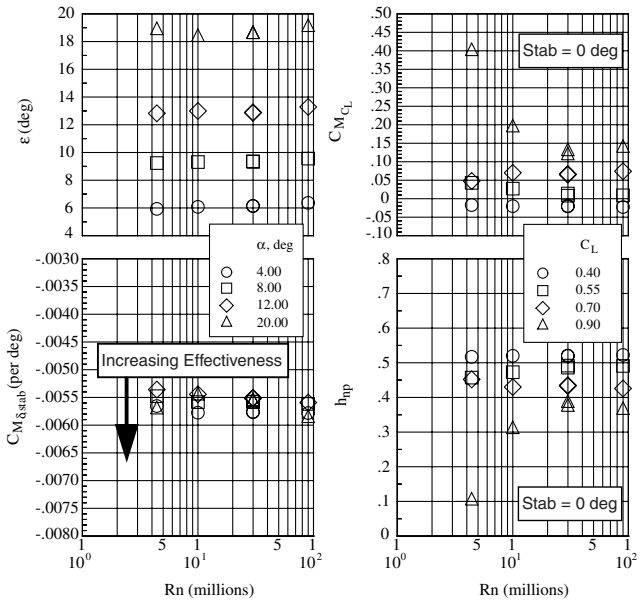

Fig. 8 Reynolds number effect on longitudinal stability and control parameters for landing configuration (corrected for static aeroelastic effect) at $M = 0.30$.

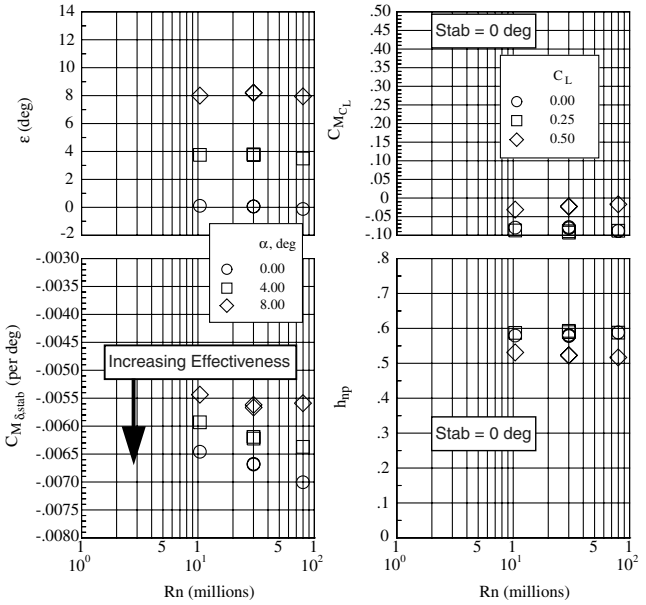

Fig. 9 Reynolds number effect on longitudinal stability and control parameters for transonic configuration (corrected for static aeroelastic effect) at $M = 0.95$.

(thinning fuselage and stab boundary layers) are shown to be the primary cause of the stab effectiveness variation as the Reynolds number changes. These thinning boundary layers expose more of the actual horizontal tail geometry to the flow, making it more effective as the Reynolds number increases. The increased exposure of the tail geometry occurs through increased exposed surface area (less fuselage boundary layer blanketing tail/fuselage juncture), increased camber (tail surface boundary layers are thinner, hiding less of the curvature of the airfoil section), and reduced airfoil thicknesses (tail airfoil sections not covered with thick boundary layers).

The plots on the right side of Fig. 8 present the local pitch stability and neutral point trends with the Reynolds number for constant values of C_L. For C_L values larger than 0.45, the landing configuration exhibits an unstable longitudinal condition, as discussed previously. Just before the onset of the model nose-up condition, the local pitch stability is insensitive to changes with the Reynolds number, as is shown for $C_L = 0.4$ in Fig. 8. Right after the nonlinear onset, $C_L = 0.45$, the increase in Reynolds number produces increased pitch stability as the onset of the nose-up pitching moment is delayed. Moving deeper into the pitch nonlinearity, the local C_M values are changing rapidly and the local pitching-moment slopes should be viewed more qualitatively. However, from this qualitative viewpoint, the pitch stability also appears to be increasing with increases in the Reynolds number.

The neutral point behavior with changing Reynolds numbers is also shown in Fig. 8. Note that these values were calculated from the local pitching-moment slopes and the same qualitative view should be considered for the higher C_L values.

The basic longitudinal stability and control parameters calculated from data (with static aeroelastic corrections) for the transonic configurations are shown in Fig. 9. The downwash angle, the pitch stability, and the neutral point show no significant dependence on the Reynolds number. However, the stabilizer effectiveness for this configuration shows a strong dependence on the Reynolds number. This trend with the Reynolds number is also consistent with the stabilizer effectiveness increase seen in subsonic transport data [25]. Both the values shown here and those presented in [25] demonstrate 10% increases in stabilizer effectiveness as the Reynolds number increases from that of a wind-tunnel-model scale to that of flight scale. This increase in stabilizer effectiveness at higher Reynolds number results from changes in the viscous effects (thinning fuselage and stabilizer boundary layers) [25]. The thinner boundary layers expose more of the actual horizontal tail geometry to the flowfield, making it more effective.

Directional Characteristics

Next, the discussion focuses on the directional stability and control characteristics. The reader is reminded that none of the data that follow have static aeroelastic corrections applied, because the resource limitations did not allow a complete set of these data to be collected.

Figure 10 shows the Reynolds number effects on the yawing moment for the landing configuration with and without chines. These α sweeps were obtained with $\beta = 0$ deg. The landing configuration tested without the forebody chines demonstrated a strong yawing moment departure at high α that is dependent on the Reynolds number. The forebody flowfield is symmetric at $Rn = 4.5 \times 10^6$ and no yawing-moment departure is observed for the given α range. Increasing the Rn to 10×10^6 causes a strong yawing-moment asymmetry to develop. Further increases in Reynolds number move the onset of this departure characteristic to lower α. The lack of a fixed separation line associated with the chines for the shed forebody vortices produces this dependence on the Reynolds number. The addition of forebody chines to the landing configuration greatly reduced the magnitude of the yawing moment departure and reduced the Reynolds number dependence by providing a fixed line of separation for the forebody vortices at high α, making the forebody flow more symmetric.

The Reynolds number effects on the directional characteristics for several landing configurations are shown in Fig. 11 at $\alpha = 12$ deg, before the onset of the previously discussed yawing-moment departure. The vertical tail provides a strong input to the directional stability at this α. Also note that with or without the vertical tail present, the forebody chines provide an additional increase in the directional stability. This significant increase in the directional stability with the addition of the chines suggests that the chine vortex on the windward side of the forebody becomes stronger. An asymmetric forebody flowfield is produced creating a side-to-side pressure difference on the forebody, which generates the observed restoring yawing moment associated with the increased directional stability. However, the directional stability still drops significantly when the vertical tail is removed. At this α, these configurations show small Reynolds number effects that tend to be greater at the larger β.

The Reynolds number effects on the directional characteristics for the same set of landing configurations are shown in Fig. 12 at $\alpha = 20$ deg, after the onset of the previously discussed yawing-moment departure. The configurations without the forebody chines exhibit a severe directional instability at $\beta = 0$ deg. This severe directional instability is caused by asymmetric vortex shedding from the forebody that switches the dominant vortex from one side to the other near $\beta = 0$ deg. The addition of the chines eliminates the strong instability at $\beta = 0$ deg, but the vertical tail is still necessary to give the configuration any directional stability at all. However, at this α the vertical tail does not appear to be as effective in providing directional stability, as it was at lower α, presumably, due to the blanketing effect attributed to the wakes of both the fuselage and wing. The Reynolds number effects on the directional characteristics are seen throughout the β range at this α. These effects should be carefully considered because of the highly unsteady nature of the flowfield at this high α condition.

The directional stability derivatives for both the landing and the transonic configurations are shown in Fig. 13. These slopes were

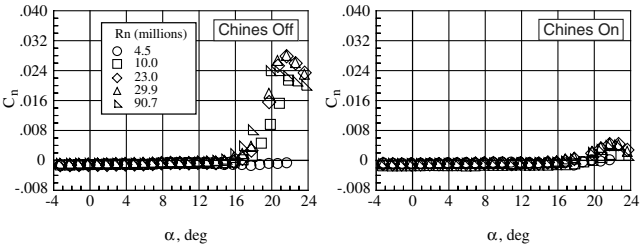

Fig. 10 Reynolds number and forebody chine effect on yawing moment departure for landing configurations; $M = 0.30$ and $\beta = 0$ deg (no static aeroelastic correction).

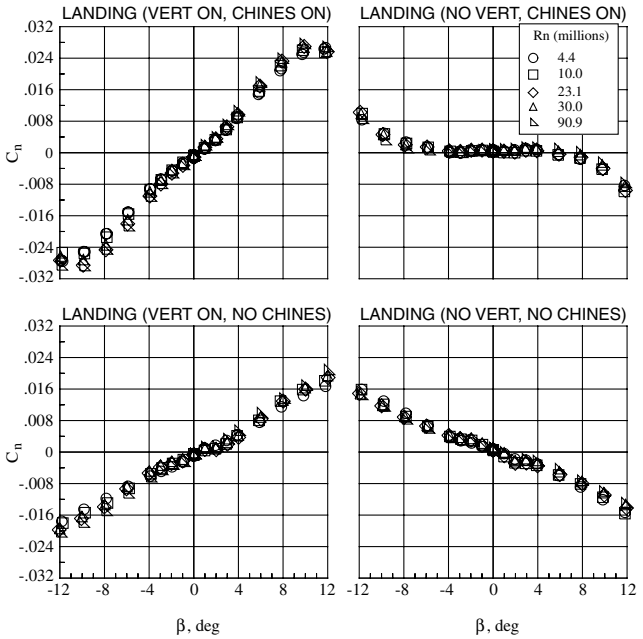

Fig. 11 Reynolds number effect on yawing-moment coefficient for various high-lift configurations; $\alpha = 12$ deg and $M = 0.30$ (no static aeroelastic correction).

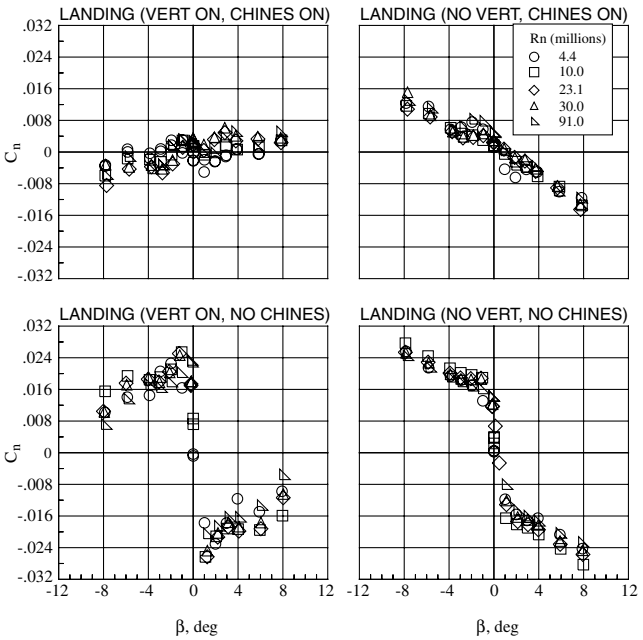

Fig. 12 Reynolds number effect on yawing-moment coefficient for various high-lift configurations; $\alpha = 20$ deg and $M = 0.30$ (no static aeroelastic correction).

calculated from data similar to that presented in Figs. 11 and 12. As mentioned previously, these derivatives were calculated based on data from a limited β range ($-4\,\text{deg} < \beta < 4\,\text{deg}$). One factor in limiting this range was the consideration of the positive interference effect caused by the presence of the blade support sting for the model. It is assumed that the blade sting with forced boundary-layer transition will produce an interference effect that will have minimal Reynolds number dependence.

Figure 13a presents the directional stability derivatives for the landing configuration as a function of α and Reynolds number. In general, the increase in Reynolds number tended to provide on the order of a 10% increase in the directional stability for this configuration. Note that due to the nonlinear and highly unsteady

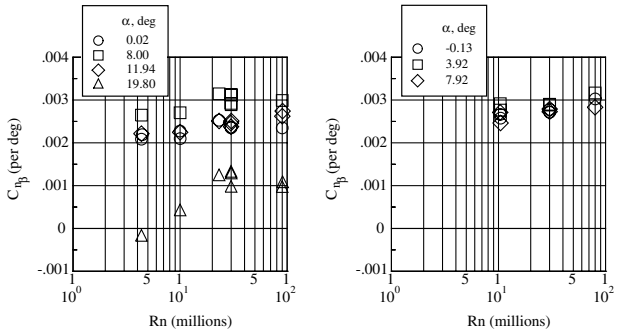

a) Landing (Vert On, Chines On), M=0.3 **b) Transonic (Vert On, Chines On), M=0.95**

Fig. 13 Reynolds number effect on directional stability (no static aeroelastic corrections).

nature of the $\alpha = 20$ deg flowfield, the data at this α should only be considered qualitatively. Figure 13b presents similar data for the transonic configuration. These data also show increases in directional stability on the order of 10% with increases in Reynolds number approaching flight conditions. The magnitude of the increase in the directional stability is similar to the magnitude of the increase in the stab effectiveness observed in the longitudinal data presented in Figs. 8 and 9. As discussed in [25], the stab effectiveness varies with changes in viscous effects (boundary-layer thicknesses) as the Reynolds number increases. Therefore, it is reasonable to assume that similar effects are involved in the changes in the directional stability shown in Fig. 13. So the increase in the directional stability at higher Reynolds number is the result of thinning fuselage and vertical tail boundary layers exposing more of the actual vertical tail geometry to the flowfield, making it more effective.

The Reynolds number effects on the directional characteristics of the landing configuration with and without rudder deflection are presented in Fig. 14. The C_n data for the configuration with no rudder deflection exhibit a slight nonlinearity near $\beta = 0$ deg that tends to go away as the Reynolds number increases. For the configuration with a +30- deg rudder deflection, a stability reversal occurs at $\beta = 1$ deg, which disappears as the Reynolds number approaches flight conditions. In an attempt to understand the nature of this nonlinearity, some simplified calculations were made on a thin airfoil with a simple hinged +30- deg TE flap (rudder) deflection using a 2-D Navier–Stokes code (FUN2D). Preliminary results of the computational study suggest a possible source for the nonlinear character in the rudder-deflected data. A key feature in this phenomenon appears to be the hinge-line radius for the rudder. For this computational analysis, the Reynolds number (based on the vertical tail chord of 5 in.) ranged from 0.9 to 19.8×10^6 at a Mach

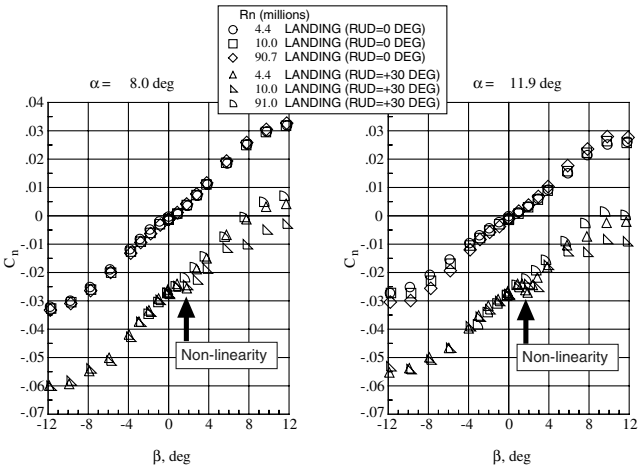

Fig. 14 Reynolds number effect on yawing-moment coefficient for landing configurations (chines on) with/without rudder deflection; $M = 0.30$ (no static aeroelastic correction).

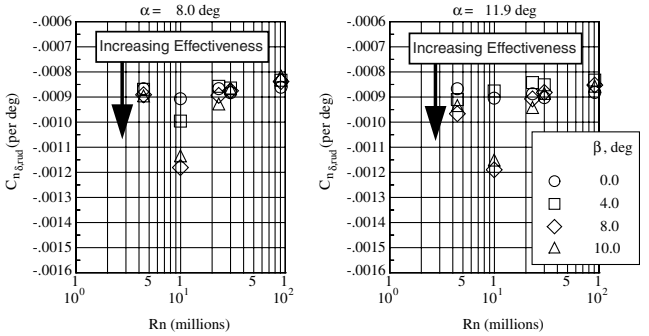

Fig. 15 Reynolds number effect on rudder effectiveness for landing (chines on) configurations; $M = 0.30$ (no static aeroelastic correction).

number of 0.3. The airfoil was also analyzed at $\alpha = -2$ deg to correspond to a $\beta = +2$ deg condition for the vertical tail on the wind-tunnel model. The analysis showed that the more negative C_n value (i.e., higher C_Y or side force on the vertical tail) for the low Reynolds number case compared with the high Reynolds number case was potentially caused by an unsteady TE flap flow separation that becomes steady at the higher Reynolds number. If this hinge line was made sharp in the computational model, then both the low Reynolds number and the high Reynolds number cases produced a steady TE flap flow separation. From this preliminary analysis, it is hypothesized that the source of this nonlinear character in the rudder-deflected data is associated with an unsteady hinge-line separation on the rudder at low Reynolds number that becomes steady at Reynolds number approaching flight. However, no dynamic wind-tunnel data are available from the NTF HSR tests to determine if unsteady rudder flow at the lower Reynolds number conditions corresponded to the occurrence of this nonlinearity in the C_n rudder data.

Finally, the effects of the Reynolds number on the rudder effectiveness are presented in Fig. 15 for the landing configuration. In general, the rudder effectiveness decreases slightly as the Reynolds number increases. This decrease may possibly be the result of static aeroelastic deformation of the vertical tail at the higher Reynolds number conditions. The variation of the rudder effectiveness with β tends to decrease at the higher Reynolds number test conditions. However, this variation shows a significant increase at a $Rn = 10 \times 10^6$, especially at the larger β values. By looking back at the C_n data for the rudder configuration shown in Fig. 14, the $Rn = 10 \times 10^6$ data appear to have a second nonlinear break at a $\beta > 6$ deg. This second break in the C_n data appears to be the source of the increased rudder effectiveness at $Rn = 10 \times 10^6$. Because this second break occurs at higher β values, the potential for some strong interaction with the blade-sting interference flowfield must be considered. However, there may also be some unsteady rudder hinge-line flow effects (see the computational analysis discussion previously) that are contributing to this variation in rudder effectiveness.

Conclusions

A high Reynolds number wind-tunnel test was conducted to assess Reynolds number effects on the stability and control characteristics of a realistic second-generation supersonic transport concept. Wind-tunnel tests with a 2.2% scale HSCT model were conducted in the NTF at NASA LARC across a wide range of Reynolds numbers. These Reynolds numbers ranged from that available in conventional wind tunnels to near-flight condition at subsonic and transonic Mach numbers. Results were presented that focus on the Reynolds number sensitivities of the stability and control characteristics at $M = 0.30$ and 0.95 for the full configuration with the empennage. General conclusions are summarized as follows:

1) The α where the pitching-moment departure occurred increased with higher Reynolds numbers.

2) The stabilizer effectiveness increased with higher Reynolds numbers for both the landing and the transonic configurations. This increase was larger for the transonic configuration than for the landing configuration. Thinning boundary layers exposed more of the stabilizer geometry, making it more effective.

3) The forebody chines supplied a strong favorable increment to C_{n_β} at higher α in the landing configuration. The α where the onset of a strong yawing-moment departure occurred decreased with higher Reynolds numbers for the landing configuration without chines at $\beta = 0$ deg.

4) Directional stability increased with higher Reynolds numbers for both the landing and the transonic configurations. Thinning boundary layers exposed more of the vertical tail geometry, making it more effective.

5) Directional stability in the landing configuration exhibited some nonlinear characteristics in β with the rudder-deflected $+30$ deg and becomes unstable between β of 1 and 2 deg at lower Reynolds number. This nonlinear characteristic is eliminated at the highest Reynolds number tested.

6) The Reynolds number effects on the stability and control characteristics for these configurations were consistent and considered reasonable. However, the development of better test techniques (i.e., model support sting system) to obtain high Reynolds number, high-load data is needed for future testing efforts.

Acknowledgments

The authors would like to thank our many partners from industry and the staff of the National Transonic Facility for making these tests successful. In particular, we would like to acknowledge Chet Nelson (Boeing), Susan Williams (NASA, retired), and Ray Gentry (NASA, retired), who invested considerable effort over many years toward the development and testing of this model. Also, discussions with Dave Bogue (Boeing) were very helpful in the analysis of the data in this paper. Finally, we would like to thank Elwood Putnam (NASA, retired) for his leadership and encouragement (especially to publish), without which this work would have been greatly limited.

References

[1] McKinney, L. W., and Baals, D. D. (eds.), "Wind Tunnel/Flight Correlation: 1981," NASA CP 2225, Nov. 1981.

[2] Haines, A. B., "Scale Effects on Aircraft and Weapon Aerodynamics," AGARD AG-323, 1994.

[3] Goldhammer, M. E., and Steinle, F. W., Jr., "Design and Validation of Advanced Transonic Wings Using CFD and Very High Reynolds Number Wind Tunnel Testing," International Council of the Aeronautical Sciences, Paper 90-2.6.2, Sept. 1990.

[4] Lynch, F. T., "Experimental Necessities for Subsonic Transport Configuration Development," AIAA Paper 92-0158, Jan. 1992.

[5] Bushnell, D. M., Yip, L. P., Yao, C. S., Lin, J. C., Lawing, P. L., Batina, J. T., Hardin, J. C., Horvath, T. J., Fenbert, J. W., and Domack, C. S., "Reynolds Number Influences in Aeronautics," NASA TM 107730, May 1993.

[6] Wilhite, A. W., and Shaw, R. J., "An Overview of NASA's High-Speed Research Program," International Council of the Aeronautical Sciences, Paper 00-112, 2000.

[7] Nelson, C. P., "Effects of Wing Planform on HSCT Off-Design Aerodynamics," AIAA Paper 92-2629, June 1992.

[8] Gloss, B. B., "Current Status and Some Future Test Directions for the U.S. National Transonic Facility," *Wind Tunnels and Wind Tunnel Test Techniques*, Royal Aeronautical Society, London, 1992, pp. 3.1–3.7.

[9] Igoe, W. B., "Analysis of Fluctuating Static Pressure Measurements in the National Transonic Facility," NASA TP-3475, Mar. 1996.

[10] Bobbitt, C. W., Hemsch, M. J., and Everhart, J. L., "NTF Characterization Status," AIAA Paper 2001-755, Jan. 2001.

[11] Fuller, D. E., "Guide for Users of the National Transonic Facility," NASA TM-83124, 1981.

[12] Owens, L. R., and Wahls, R. A., "Reynolds Number Effects on a Supersonic Transport at Subsonic Conditions," AIAA Paper 2001-0911, Jan. 2001.

[13] Wahls, R. A., Owens, L. R., and Rivers, S. M. B., "Reynolds Number Effects on a Supersonic Transport at Transonic Conditions," AIAA Paper 2001-0912, Jan. 2001.

[14] Owens, L. R., Wahls, R. A., and Rivers, S. M., "Off-Design Reynolds Number Effects for a Supersonic Transport," *Journal of Aircraft*, Vol. 42, No. 6, Nov.–Dec. 2005, pp. 1427–1441.

[15] Owens, L. R., Wahls, R. A., Elzey, M. B., and Hamner, M. P.,

"Reynolds Number Effects on the Stability & Control Characteristics of a Supersonic Transport," AIAA Paper 2002-0417, Jan. 2002.
[16] Finley, T. D., and Tcheng, P., "Model Attitude Measurements at NASA Langley Research Center," AIAA Paper 92-0763, 1992.
[17] Londenberg, W. K., "Computational Assessment of Aft-Body Closure for the Reference H Configuration," NASA CR-1999-209521, Nov. 1999.
[18] Foster, J. M., and Adcock, J. B., "User's Guide for the National Transonic Facility Research Data System," NASA TM-110242, Apr. 1996.
[19] Williams, M. S., "Experience with Strain Gage Balances for Cryogenic Wind Tunnels," AGARD R-774, 1989, pp. 18.1–18.14.
[20] Buehrle, R. D., Young, C. P., Jr., Balakrishna, S., and Kilgore, W. A., "Experimental Study of Dynamic Interaction Between Model Support Structure and a High Speed Research Model in the National Transonic Facility," AIAA Paper 94-1623-CP, 1994.
[21] Braslow, A. L., and Knox, E. C., "Simplified Method for Determination of Critical Height of Distributed Roughness Particles for Boundary-Layer Transition at Mach Numbers from 0 to 5," NACA TN-4363, 1958.
[22] Wahls, R. A., Adcock, J. B., Witkowski, D. P., and Wright, F. L., "A Longitudinal Aerodynamic Data Repeatability Study for a Commercial Transport Model in the National Transonic Facility," NASA TP-3522, Aug. 1995.
[23] Wahls, R. A., Gloss, B. B., Flechner, S. G., Johnson, W. G., Jr., Wright, F. L., Nelson, C. P., Nelson, R. S., Elzey, M. B., and Hergert, D. W., "A High Reynolds Number Investigation of a Commercial Transport Model in the National Transonic Facility," NASA TM-4418, Apr. 1993.
[24] Al-Saadi, J. A., "Effect of Reynolds Number, Boundary-Layer Transition, and Aeroelasticity on Longitudinal Aerodynamic Characteristics of a Subsonic Transport Wing," NASA TP-3655, Sept. 1997.
[25] Reichenbach, S. H., and McMasters, J. H., "A Semiempirical Interpolation Technique for Predicting Full-Scale Flight Characteristics," AIAA Paper 87-0427, Jan. 1987.